



Penta-channel waveguide-based near-eye display with two-dimensional pupil expansion

Chao Ping Chen, Xiaojun Wu, Jinfeng Wang, Baoen Han, Yunfan Yang, Shuxin Liu*

State Key Laboratory of Avionics Integration and Aviation System-of-Systems Synthesis, School of Electronic Information and Electrical Engineering, Shanghai Jiao Tong University, Shanghai, China

ARTICLE INFO

Keywords:

Metaverse
Augmented reality
Near-eye display
Waveguide
Multi-channel
Pupil expansion

ABSTRACT

We present a penta-channel waveguide-based near-eye display as an ultra-wide-angle architecture for the metaverse. The core concept is to divide one field of view into five by placing the couplers within the regions, where only the subsets of field of view are located. Compared to its counterparts, including the single, double, triple and quad channels, our penta-channel waveguide can push the envelope of field of view further. With the aid of k -space diagram, the upper limit of field of view is illustrated and deduced. The design rules of the waveguide, 4-level grating as the in-coupler, and two-dimensional binary grating as the out-coupler are expounded. Through the rigorous coupled-wave analysis, the efficiencies of gratings can be calculated and optimized. As an overall evaluation, its key performance indicators are summarized as follows. Field of view is 109° (diagonal), eye relief is 10 mm, exit pupil is $6.2 \times 6.2 \text{ mm}^2$, and pupil uniformity is 54 %.

1. Introduction

Over the last three years, we have been witnessing a dramatic rise and fall of metaverse [1]. Its hype peaked in 2021 when Facebook was renamed as Meta and begun to cool down as soon as ChatGPT was released in 2022, pivoting the public attention to artificial intelligence (AI). Per Crunchbase, total metaverse investment in 2023 fell to \$1.97 billion, down 66% from its 2021 peak [2]. This flash crash prompts us to wonder what went wrong with metaverse. Macroeconomic factors and other hardware components aside, we shall dig into near-eye displays (NEDs) and understand how the metaverse is beset by two paradoxes arising from this type of hardware. Paradox 1: the way NEDs are used contradicts the fact that people tend to not put clunky things on their heads. Especially for things weighing a few hundred grams. To solve this paradox, we must either reduce the weight, or give them a must-have, such as vision correction [3]. Otherwise, nobody wants a head-worn device. Paradox 2: a negative correlation between performance and design. For starters, to have a big field of view (FOV) for immersion, we will need to enlarge the microdisplay or to shorten the focal length [4]. To have a high-fidelity image, we will need more lenses or other optical elements to fix all sorts of aberrations [5]. To have a large exit pupil or eye box, we will need to increase the lens aperture [6]. Unfortunately,

all of these will only add up to a bulkier or more complicated design, which could be a deal breaker for many.

If have to sum up the evolution of NEDs into just one phrase, it would be “get slimmer”. Of various efforts to slim down, the most effective one is arguably to fold the light path. One example is pancake lenses [7–9], which are being widely adopted in the non-transparent or virtual reality (VR) NEDs, e.g., Apple Vision Pro. Another example is waveguides [10–17], commonly seen in the transparent or augmented reality (AR) NEDs, e.g., Microsoft HoloLens 2. As to which one is better, it is obviously the pancake lenses, when it comes to FOV, image quality and supply chain. But in the long run, we still see in the latter a chance to turn around. For now, the biggest hurdle for waveguides is the small FOV. As a comparison, HoloLens 2 has a FOV of 52° , while Vision Pro 100 to 110° [18]. However, HoloLens 2 debuted a concept known as FOV division [19]. Later, inspired by this concept, dual-channel [20–23], triple-channel [24], and quad-channel [25] waveguides were proposed. As a further step, we hereby present a penta-channel waveguide-based NED, whose FOV is split into five. In the ensuing sections, we will walk through its design, principles, and key performance indicators.

* Corresponding author.

E-mail address: liushuxin@sjtu.edu.cn (S. Liu).

<https://doi.org/10.1016/j.displa.2025.102999>

Received 23 January 2025; Received in revised form 12 February 2025; Accepted 16 February 2025

Available online 17 February 2025

0141-9382/© 2025 Elsevier B.V. All rights are reserved, including those for text and data mining, AI training, and similar technologies.

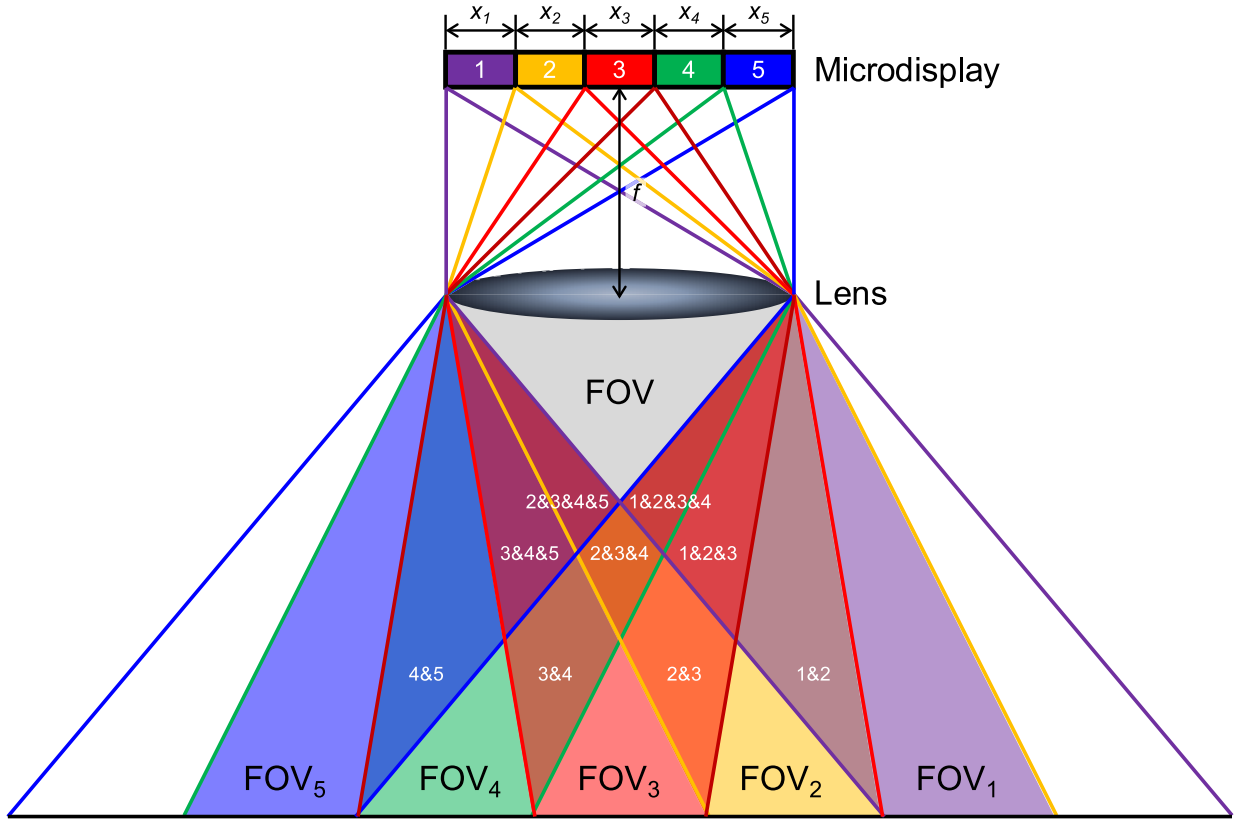


Fig. 1. Illustration of FOV division. Picture a microdisplay being segmented into 5 zones and located at a focal length f away from a lens. By drawing out rays emitting from the boundaries of each zone, a total of 15 regions or combinations of different FOVs could be identified. The gray triangular region right beneath the lens is where all FOVs overlap. The light purple, yellow, red, green and blue regions are exclusive to $FOV_{1/2/3/4/5}$, respectively.

2. Design rules

2.1. FOV division

To illustrate how the FOV is divided, as shown in Fig. 1, picture a microdisplay being segmented into 5 zones and located at a focal length f away from a lens. Let the FOV of zone 1/2/3/4/5 be denoted as $FOV_{1/2/3/4/5}$. By drawing out rays emitting from the boundaries of each zone, a total of 15 regions or combinations of different FOVs could be identified. The gray triangular region right beneath the lens is where all FOVs overlap. Customarily, when an optical designer thinks of FOV, this is the region he/she will relate to. But in our case, we turn our attention to the light purple, yellow, red, green and blue regions, which are exclusive to $FOV_{1/2/3/4/5}$, respectively. Compared to other FOV division techniques [19–25], the proposed one could enable more channels that were not possible before. For instance, the polarization-based FOV division can merely offer 2 channels [20]. Now, let the lengths of zone 1/2/3/4/5 be $x_{1/2/3/4/5}$. Thus, the $FOV_{1/2/3/4/5}$ could be written in sequence as

$$FOV_1 = \tan^{-1}\left(\frac{2x_1 + 2x_2 + x_3}{2f}\right) - \tan^{-1}\left(\frac{2x_2 + x_3}{2f}\right) \quad (1)$$

$$FOV_2 = \tan^{-1}\left(\frac{2x_2 + x_3}{2f}\right) - \tan^{-1}\left(\frac{x_3}{2f}\right) \quad (2)$$

$$FOV_3 = 2\tan^{-1}\left(\frac{x_3}{2f}\right) \quad (3)$$

$$FOV_4 = \tan^{-1}\left(\frac{2x_4 + x_3}{2f}\right) - \tan^{-1}\left(\frac{x_3}{2f}\right) \quad (4)$$

Table 1

Parameters for microdisplay.

| Panel model | Parameter | Value |
|----------------|-------------------------|----------------------|
| Sony ECX343ENA | diagonal size | 0.68 in. (17.272 mm) |
| | horizontal size | 14.647 mm |
| | vertical size | 9.154 mm |
| | resolution | 1920 × 1200 |
| | aspect ratio | 1.6 |
| | distance to lens or f | 6.145 mm |
| | x_1 | 3.775 mm |
| | x_2 | 2.464 mm |
| | x_3 | 2.167 mm |
| | x_4 | 2.464 mm |
| x_5 | 3.775 mm | |

$$FOV_5 = \tan^{-1}\left(\frac{2x_4 + 2x_5 + x_3}{2f}\right) - \tan^{-1}\left(\frac{2x_4 + x_3}{2f}\right) \quad (5)$$

2.2. Microdisplay

To practice the above concept and without loss of generality, we shall exemplify with an organic light-emitting diode-on-silicon microdisplay (Sony ECX343ENA) [26]. The same design rules also apply to other self-emissive microdisplays, e.g., light-emitting diode [27]. Its parameters are itemized in Table 1, where the resolution is WUXGA (1920 × 1200), aspect ratio 1.6, panel size 0.68 in. (14.647 × 9.154 mm²), and distance to lens (i.e., focal length f) 6.145 mm. The latter two parameters will translate to a FOV of 109° (100° × 73°). For FOV to be equally divided in the horizontal direction, revisiting Eqs. (1)–(5), we shall set $x_{1/2/3/4/5}$ to 3.775/2.464/2.167/2.464/3.775 mm. In this case, $FOV_{1/2/3/4/5} = 20^\circ$.

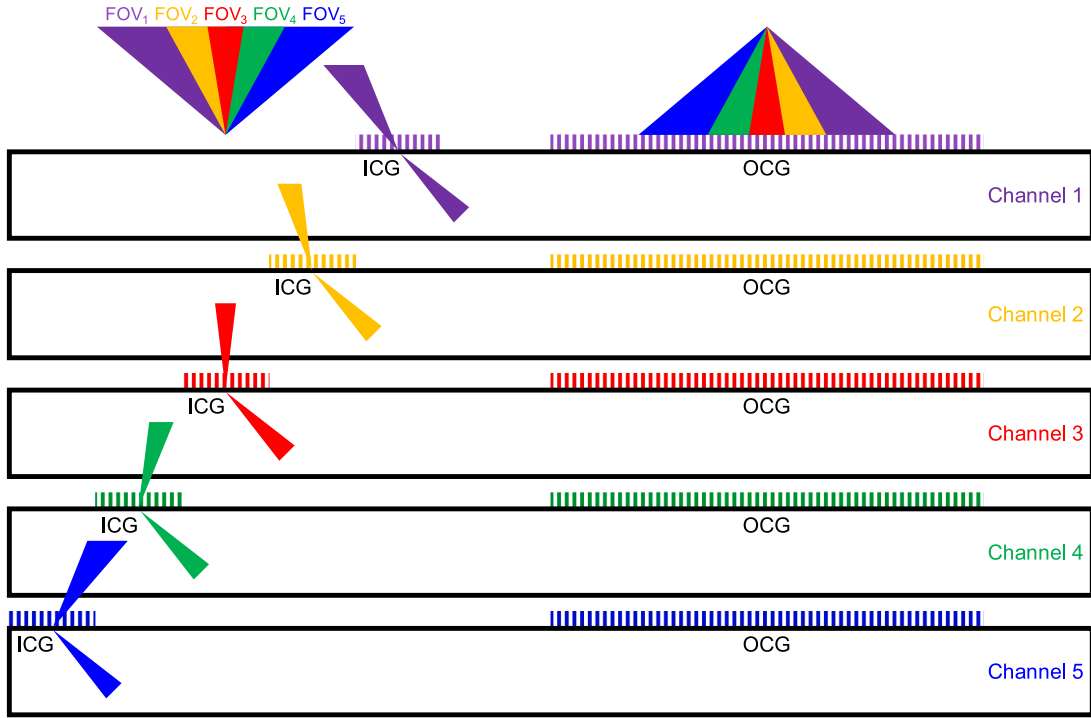


Fig. 2. Cross-section of penta-channel waveguide. Unlike the orthodox waveguide designs, where ICGs are placed within the region of FOV, our design places ICGs within the regions of $FOV_{1/2/3/4/5}$ so that $FOV_{1/2/3/4/5}$ could be exclusively coupled into their respective channels.

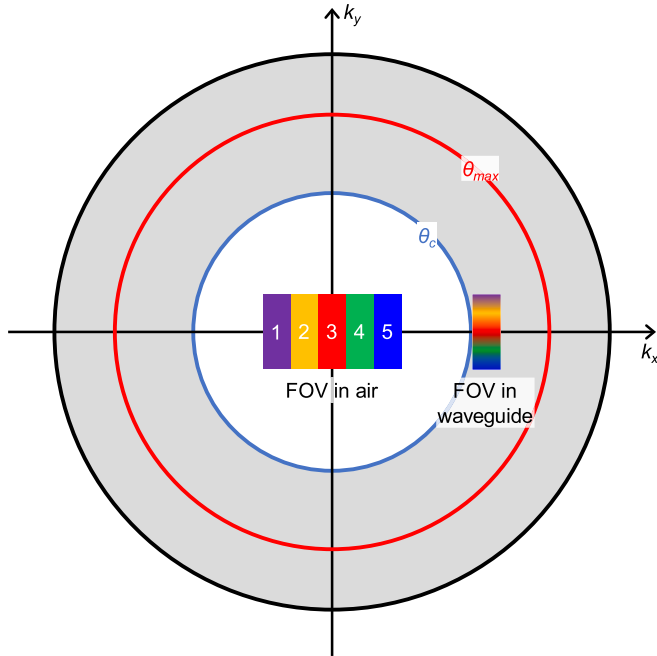


Fig. 3. Transition of FOV from air to waveguide in k -space diagram. The FOV in air is divided into five sub-FOVs along the horizontal direction. After entering the waveguide, all sub-FOVs are supposed to overlap each other and to be tangent to the innermost circle.

2.3. Penta-channel waveguide

Fig. 2 shows a cross-section of the proposed penta-channel waveguide, with its five layers being labeled as channel 1/2/3/4/5. Both in-coupling gratings (ICGs) and out-coupling gratings (OCGs) are operated in transmissive mode. Unlike the orthodox waveguide designs, where

ICGs are placed within the region of FOV, our design places ICGs within the regions of $FOV_{1/2/3/4/5}$ so that $FOV_{1/2/3/4/5}$ could be exclusively coupled into their respective channels. As a result, ICGs are misaligned rather than center-aligned. Considering the efficiencies of ICGs cannot reach 100%, this misalignment of ICGs is particularly beneficial because it prevents a channel from being affected by its adjacent channel. The downside is that bigger waveguides are needed to accommodate these ICGs. As to the waveguide material, a lanthanum dense flint glass LASF35 (Schott) is chosen, whose refractive index n_{wg} at 633/546/486 nm is 2.0149/2.0304/2.0471, yielding to a critical angle θ_c of $29.76^\circ/29.51^\circ/29.25^\circ$.

2.4. Upper limit of FOV

By means of wave vector or k -space diagram—a coordinate formed by the x-components (k_x) and y-components (k_y) of wave vectors—the transition of FOV from air to waveguide can be depicted as in Fig. 3. The innermost and outermost circles demarcate the ranges of wave vectors in air and waveguide, respectively. The FOV in air is divided into five sub-FOVs along the horizontal direction. After entering the waveguide, all sub-FOVs are supposed to overlap each other and to be tangent to the innermost circle. Apparently, the minimum angle in waveguide is the critical angle θ_c of total internal reflection. In the meantime, to allow a pupil to be duplicated multiple times, the maximum angle θ_{max} in waveguide, which traces out a middle red circle in k -space, shall be determined from [23]

$$\theta_{max} = \tan^{-1} \left(\frac{D_p}{2D} \right) \quad (6)$$

where D_p is the pupil diameter and D the waveguide thickness. With aspect ratio being fixed to 1.6, the upper limit of diagonal FOV, FOV_{max} , can be deduced as [24]

$$FOV_{max} = 2 \cdot \tan^{-1} \left(\sqrt{\tan^2 \left(\frac{FOV_h}{2} \right) + \tan^2 \left(\frac{FOV_v}{2} \right)} \right) \quad (7)$$

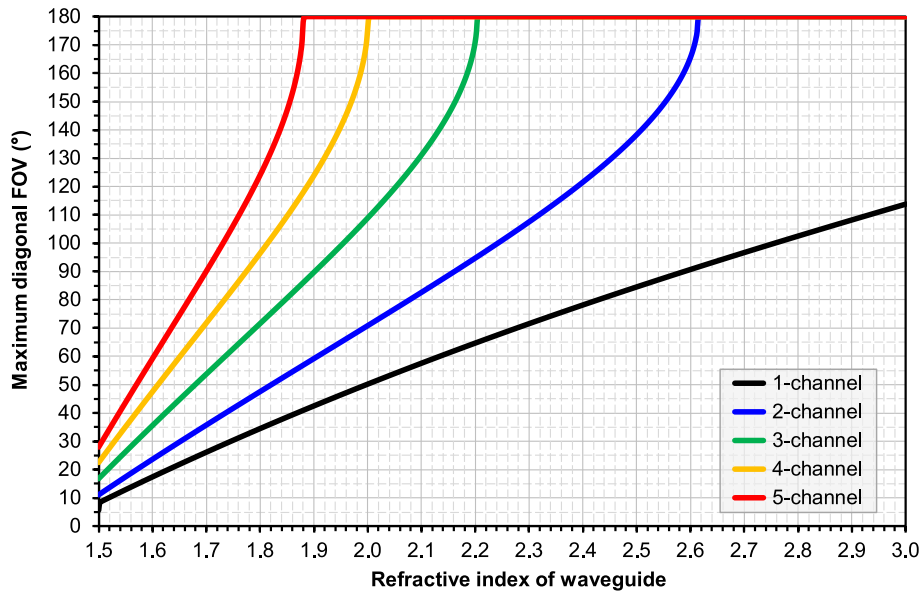


Fig. 4. Upper limit of diagonal FOV with respect to the refractive index of waveguide. When $n_{wg} = 1.8$, the upper limit of FOV is $34^\circ/48^\circ/72^\circ/96^\circ/124^\circ$ for the single/dual/triple/quad/penta-channel waveguide.

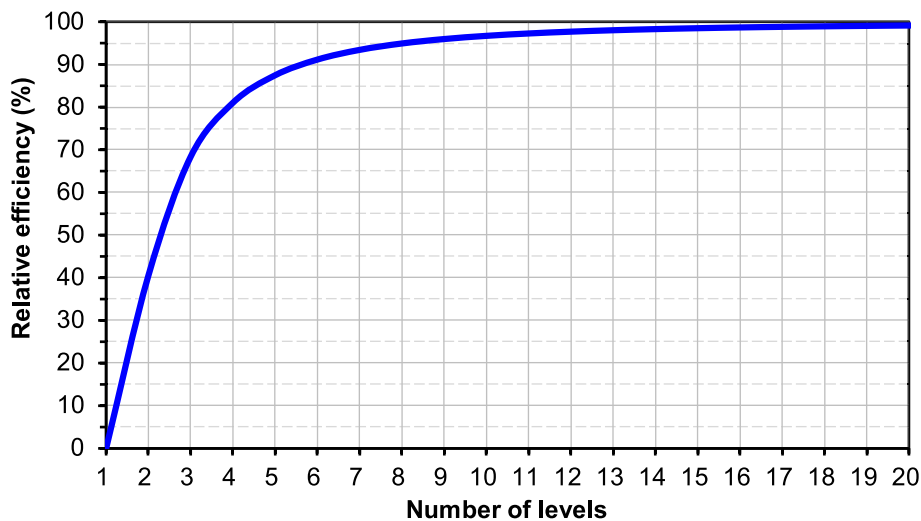


Fig. 5. Efficiency of multilevel grating relative to that of sawtooth grating. When the number of levels increases, the efficiency of multilevel grating will infinitely approach that of sawtooth grating.

where

$$FOV_h = 2 \cdot \sin^{-1} \left(\frac{n_{wg}}{n_{air}} \sin \left(\frac{N_c (\theta_{max} - \theta_c)}{2} \right) \right) \quad (8)$$

and

$$FOV_v = 2 \cdot \tan^{-1} \left(\frac{\tan(FOV_h/2)}{1.6} \right) \quad (9)$$

where FOV_h/FOV_v is the horizontal/vertical FOV, n_{air}/n_{wg} the refractive index of air/waveguide, and N_c the number of channels. Provided $D_p = 3$ mm, $D = 1.5$ mm, and $N_c = 1/2/3/4/5$, FOV_{max} can be calculated with respect to the refractive index of waveguide, as shown in Fig. 4. When $n_{wg} = 1.8$, FOV_{max} is $34^\circ/48^\circ/72^\circ/96^\circ/124^\circ$ for the single/dual/triple/quad/penta-channel waveguide.

2.5. In-coupling grating

The task of ICGs is to transfer the light from air to waveguide at a high efficiency. One solid candidate for this purpose is the blazed grating [28], which is characterized by a sawtooth profile. Interestingly, linear as it may look, blazed grating is actually approximated by a multilevel grating whether during calculation or fabrication [29]. Otherwise, grayscale or direct-write lithography is necessary. To avoid ambiguity—both gratings can be deemed as blazed as far as efficiency is concerned—the former shall be referred to as sawtooth grating hereafter. According to scalar diffraction theory, the efficiency η of the first order of a multilevel grating is given by

$$\eta = \eta_0 \left(\text{sinc}^2 \left(\frac{\pi}{N} \right) \right) \quad (10)$$

where η_0 is the efficiency of sawtooth grating and N the number of levels. As can be seen from Fig. 5, when the number of levels increases, the efficiency of multilevel grating will infinitely approach that of sawtooth

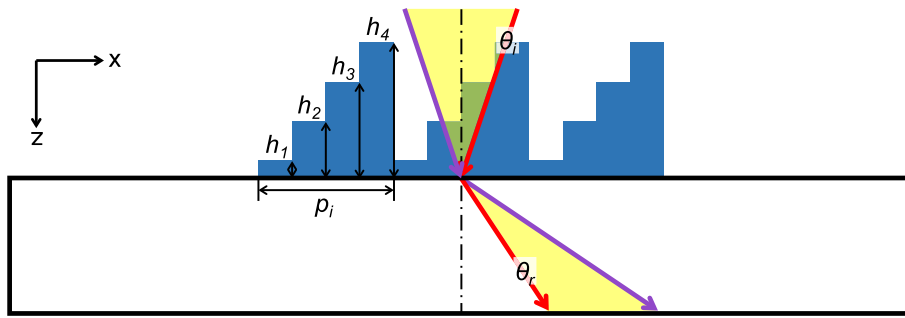


Fig. 6. Profile of in-coupling grating, which is a 4-level grating. θ_i is the incident angle, θ_r the refracted angle of the first order, p_i the grating period, and $h_{1/2/3/4}$ the grating height.

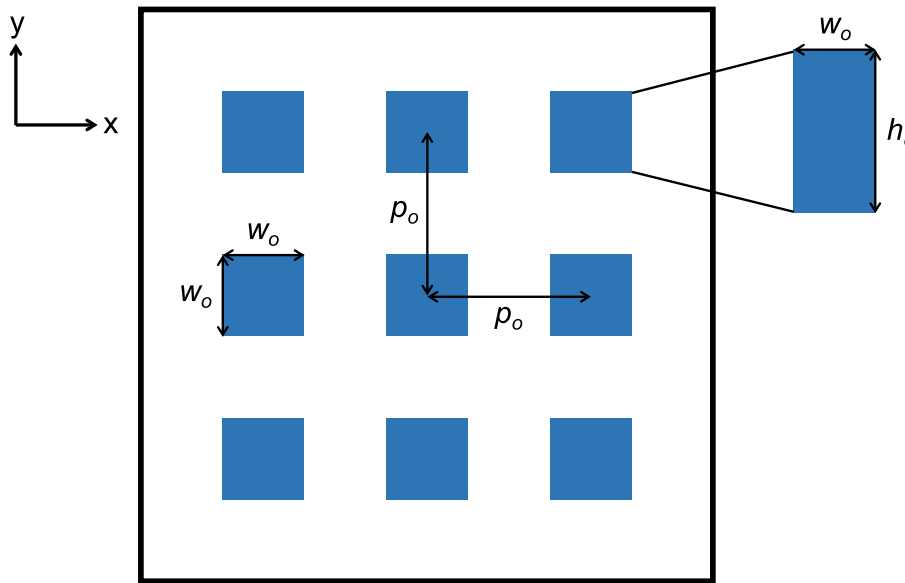


Fig. 7. Profile of 2D binary out-coupling grating, which is arranged into an array of cuboids. The grating height, widths and periods—both horizontal and vertical—are h_o , w_o and p_o , respectively.

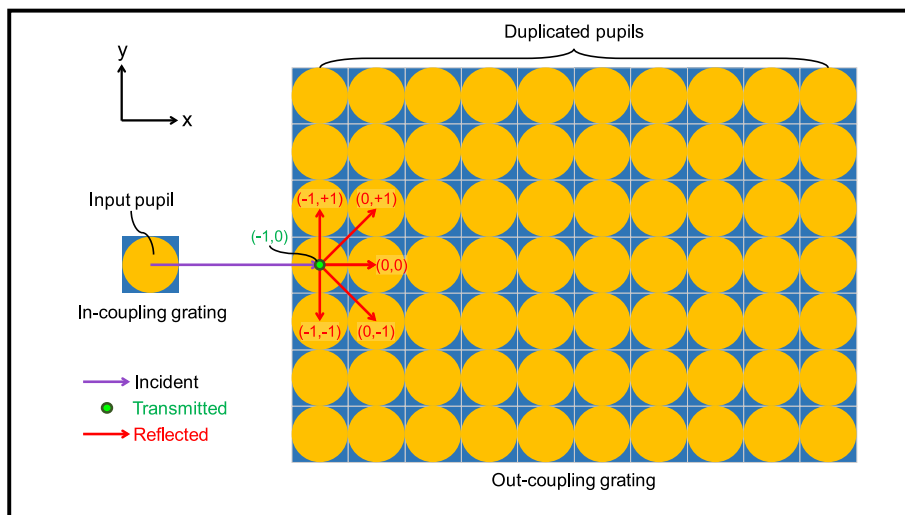


Fig. 8. Grating layout along with pupil footprints. The OCG consists of 10×7 sub-gratings. When light incident from ICG, as denoted by a purple out-of-plane arrow, hits OCG, there will be one transmitted order ($T(-1,0)$), as denoted by a green arrow, and five reflected orders ($R(0,0)$, $R(-1,+1)$, $R(-1,-1)$, $R(0,+1)$, $R(0,-1)$), as denoted by red arrows.

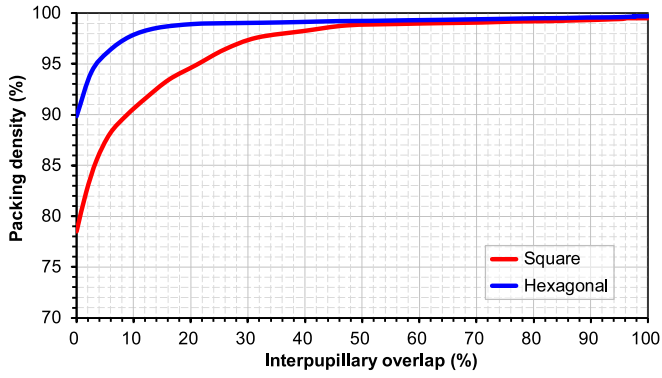


Fig. 9. When $D_p = 3$ mm and $A_{ocg} = 30 \times 21$ mm², packing density is plotted as a function of interpupillary overlap. Unsurprisingly, more pupils could be packed into hexagonal grids than into square grids. In the case of no overlapping, densities for square and hexagonal grids are 78 and 90 %, respectively.

grating. This in part explains why in the layer-based rigorous coupled-wave analysis (RCWA) [30], the calculation error of sawtooth grating can be less than 1 % if $N \geq 19$. In practice, the choice of N hinges on the technology or process node of fabrication. As a viable option, a 4-level grating is demonstrated, as shown in Fig. 6, where four grating heights $h_{1/2/3/4}$ are evenly distributed across the grating period p_i . Invoking the grating equation [22], incident angle θ_i , refracted angle θ_r of the first order, n_{air} , n_{wg} , p_i , and wavelength λ could be correlated via

$$n_{wg} \sin \theta_r - n_{air} \sin \theta_i = \frac{\lambda}{p_i} \quad (11)$$

For the sake of symmetry, we prefer to design with channel 3, which sits in the middle of FOV. To make sure all fields satisfy the total internal reflection conditions, the rightmost field ($\theta_i = -10^\circ$) shall correspond to an angle no less than the critical angle. In our case, $\theta_r = 30^\circ$. For a wavelength of 546 nm, $p_i = 459.25$ nm.

2.6. Out-coupling grating

The task of OCGs is to duplicate the pupils and to couple the light out of waveguide. For two-dimensional (2D) pupil expansion, a 2D binary grating is arranged into an array of cuboids, as shown in Fig. 7, where the grating height, widths and periods—both horizontal and vertical—are h_o , w_o and p_o , respectively. To differentiate from WaveOptics' OCG [16], whose rows are staggered, rows of our OCG are aligned. To conserve the field angle after out-coupling, the grating period of OCG equals that of ICG, i.e., $p_o = p_i$. To show how exit or output pupil is expanded, the grating layout along with pupil footprints is depicted in Fig. 8, where the OCG consists of 10×7 sub-gratings. When light incident from ICG, as denoted by a purple out-of-plane arrow, hits OCG, there will be one transmitted order (T(-1,0)), as denoted by a green arrow, and five reflected orders (R(0,0), R(-1,+1), R(-1,-1), R(0,+1), R(0,-1)), as denoted by red arrows. As OCG is x-y symmetric, R(-1,+1) and R(0,+1) shall be equivalent to R(-1,-1) and R(0,-1), respectively.

2.7. Pupil packing

Analogous to solving the circle packing problem [31]—except that our pupils are allowed to overlap and be partially cropped—we shall pack the pupils in OCG with the highest density η_p , which is defined as

$$\eta_p = \frac{A_p}{A_{ocg}} \quad (12)$$

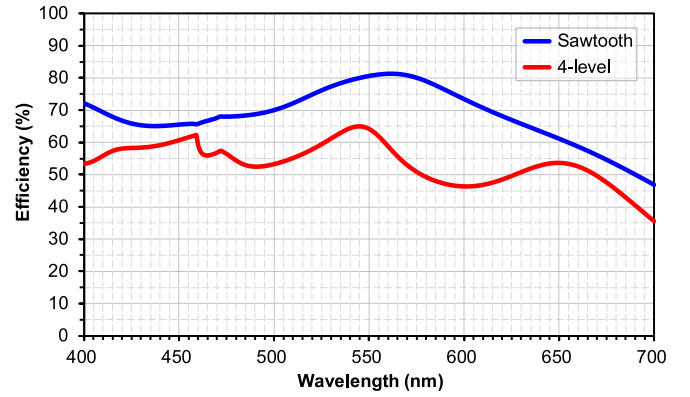


Fig. 10. In-coupling efficiency of T(+1,0) versus the wavelength. If to sum all efficiencies over the entire visible spectrum, the summed efficiency of 4-level grating is 78 % of that of sawtooth grating, proving that 4-level grating can be a decent substitute of sawtooth grating.

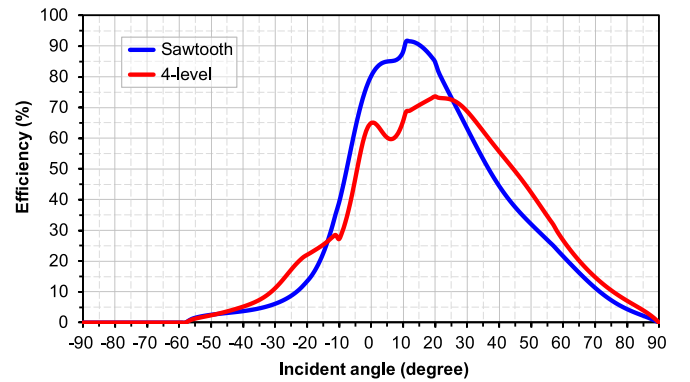


Fig. 11. In-coupling efficiency of T(+1,0) versus the incident angle. As to angular bandwidth of efficiency exceeding 50 %, sawtooth and 4-level gratings have 43° (-7° to $+36^\circ$) and 48° (-4° to $+44^\circ$), respectively.

Table 2
Parameters for the in-coupling grating in channel 3.

| Grating | Shape | Parameter | Value |
|-------------|----------|---------------|-----------|
| in-coupling | sawtooth | base material | LASF35 |
| | | p_i | 459.25 nm |
| height | | 717 nm | |
| in-coupling | 4-level | base material | LASF35 |
| | | p_i | 459.25 nm |
| | | h_1 | 0 nm |
| | | h_2 | 173.25 nm |
| | | h_3 | 346.50 nm |
| | | h_4 | 519.75 nm |

where A_p is the area covered by duplicated pupils and A_{ocg} the area of OCG. When $D_p = 3$ mm and $A_{ocg} = 30 \times 21$ mm², packing density is plotted as a function of interpupillary overlap, as shown in Fig. 9. Unsurprisingly, more pupils could be packed into hexagonal grids [16] than into square grids. In the case of no overlapping, densities for square and hexagonal grids are 78 and 90 %, respectively. For a higher density, one way is to enlarge the overlap, but at the cost of interference. Another way is to alter the shape of pupil to square since OCG itself is rectangular.

Table 3
Parameters for the out-coupling grating in channel 3.

| Grating | Shape | Parameter | Value |
|--------------|--------|---------------|----------------|
| out-coupling | cuboid | base material | LASF35 |
| | | p_o | 459.25 nm |
| | | w_o | 0 to 459.25 nm |
| | | h_o | 0 to 800 nm |

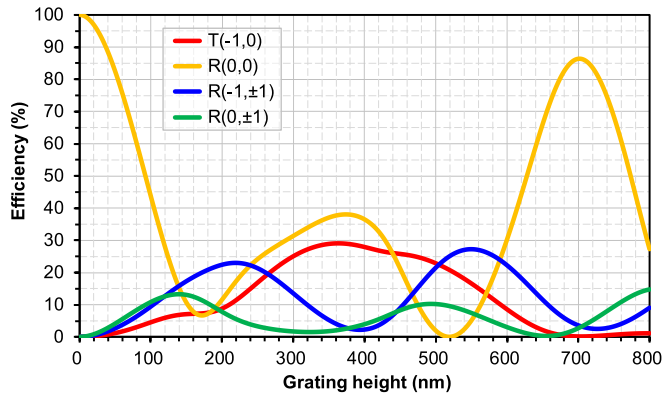


Fig. 12. When the fill factor is 50 %, efficiencies of $T(-1,0)$, $R(0,0)$, $R(-1,\pm 1)$ and $R(0,\pm 1)$ are computed against the grating height.

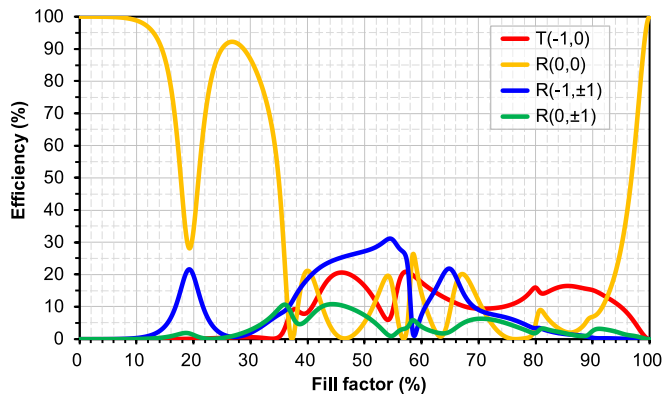


Fig. 13. When the grating height is 550 nm, efficiencies of $T(-1,0)$, $R(0,0)$, $R(-1,\pm 1)$ and $R(0,\pm 1)$ are computed against the fill factor.

3. Results and discussion

3.1. In-coupling efficiency

For grating analysis, VirtualLab Fusion (Wyrowski Photonics GmbH), which leverages RCWA method, is employed. To show the difference between sawtooth grating and its 4-level equivalent in channel 3, in-coupling efficiencies of $T(+1,0)$ versus both wavelength and incident angle are computed, as shown in Fig. 10 and Fig. 11, respectively. Parameters used are listed in Table 2. The polarization is transverse magnetic (TM) or 0° . If to sum all efficiencies over the entire visible spectrum, the summed efficiency of 4-level grating is 78 % of that of sawtooth grating, proving that 4-level grating can be a decent substitute of sawtooth grating. At wavelengths of 486/546/633 nm, efficiencies of sawtooth and 4-level gratings are 58/69/58 % and 52/61/54 %, respectively. As to spectral bandwidth of efficiency exceeding 50 %, sawtooth and 4-level gratings have 290 nm (400 to 690 nm) and 218 nm

(400 to 577 nm & 627 to 668 nm), respectively. As to angular bandwidth of efficiency exceeding 50 %, sawtooth and 4-level gratings have 43° (-7 to $+36^\circ$) and 48° (-4 to $+44^\circ$), respectively. On the whole, 4-level grating is not as good as sawtooth grating. Yet, it could outperform many other types of gratings, e.g., holographic [32,33] and liquid crystal [34,35] gratings.

3.2. Out-coupling efficiency

For OCG in channel 3, its parameters are listed in Table 3. Unlike ICG, whose energy is concentrated to one specific order, the energy of OCG is spread out. To modulate the efficiency, both the grating height and fill factor can be tweaked. To improve the uniformity, a rule of thumb is to boost $R(-1,\pm 1)$ while suppressing $R(0,\pm 1)$. As shown in Fig. 12, when the fill factor is 50 %, efficiencies of $T(-1,0)$, $R(0,0)$, $R(-1,\pm 1)$ and $R(0,\pm 1)$ are computed against the grating height. As shown in Fig. 13, when the grating height is 550 nm, efficiencies of $T(-1,0)$, $R(0,0)$, $R(-1,\pm 1)$ and $R(0,\pm 1)$ are computed against the fill factor. It can be seen that each order shall be subject to different conditions to maximize its efficiency. The maximum efficiencies of $T(-1,0)$, $R(0,0)$, $R(-1,\pm 1)$ and $R(0,\pm 1)$ are 29 %, 100 %, 31 % and 15 %, respectively.

3.3. Pupil uniformity

The pupil uniformity is quantitatively assessed with the light guide toolbox of VirtualLab Fusion. Because the FOV is equally divided and all angles to be reflected in channel 1/2/3/4/5 are identical, only the channel 3—where the FOV_3 is located—is demonstrated. Fig. 14 shows the ray tracing diagram of channel 3, where the wavelength is 546 nm, incident angle 0° , waveguide thickness 1.5 mm, and input pupil a circle with a diameter of 3 mm. The size of ICG is $3 \times 3 \text{ mm}^2$. The size of OCG is $30 \times 21 \text{ mm}^2$. The distance between ICG and OCG is 9 mm. The input FOV is 109° ($100^\circ \times 73^\circ$). Hence, if the eye relief is 10 mm, the exit pupil or eyebox will be $6.2 \times 6.2 \text{ mm}^2$. Via the parametric optimization, the efficiencies of 70 sub-gratings could be fine-tuned to minimize the uniformity error. From the electromagnetic field tracing, the intensity map of duplicated pupils can be obtained, as shown in Fig. 15. The input intensity of the source is normalized to $1 \text{ V}^2/\text{m}^2$. For the interpupillary overlaps, coherent summations of electric fields are applied. As the minimal and maximal intensities are 0.00026 and $0.00071 \text{ V}^2/\text{m}^2$, respectively, the pupil uniformity is 54 %.

4. Conclusions

To push the envelope of FOV, a penta-channel waveguide-based NED has been proposed. The following key performance indicators have been met: FOV is 109° (diagonal), eye relief is 10 mm, exit pupil is $6.2 \times 6.2 \text{ mm}^2$, and pupil uniformity is 54 %. To be clear and concise, we would like to boil down what we had done into three major contributions. Contribution 1: one more channel to the FOV division. The multi-channel waveguide is coming to the fifth iteration, i.e., penta-channel. Contribution 2: a design of 4-level grating as an alternative to the sawtooth grating. Spectral bandwidth wise, sawtooth grating wins. Angular bandwidth wise, 4-level grating wins. Contribution 3: a design of 2D pupil expander featuring an array of cuboids. Packing density as well as order-wise efficiencies has been discussed. While the FOV of waveguide-based NEDs is now on par with that of magnifier-based NEDs [36], it is still unlikely that the waveguides will take over the magnifiers in the VR sector anytime soon. That said, in the AR sector, waveguides are expected to beat other competitors, e.g., reflectors [37–39] and contact lenses [40–42], and claim the champion of this track.

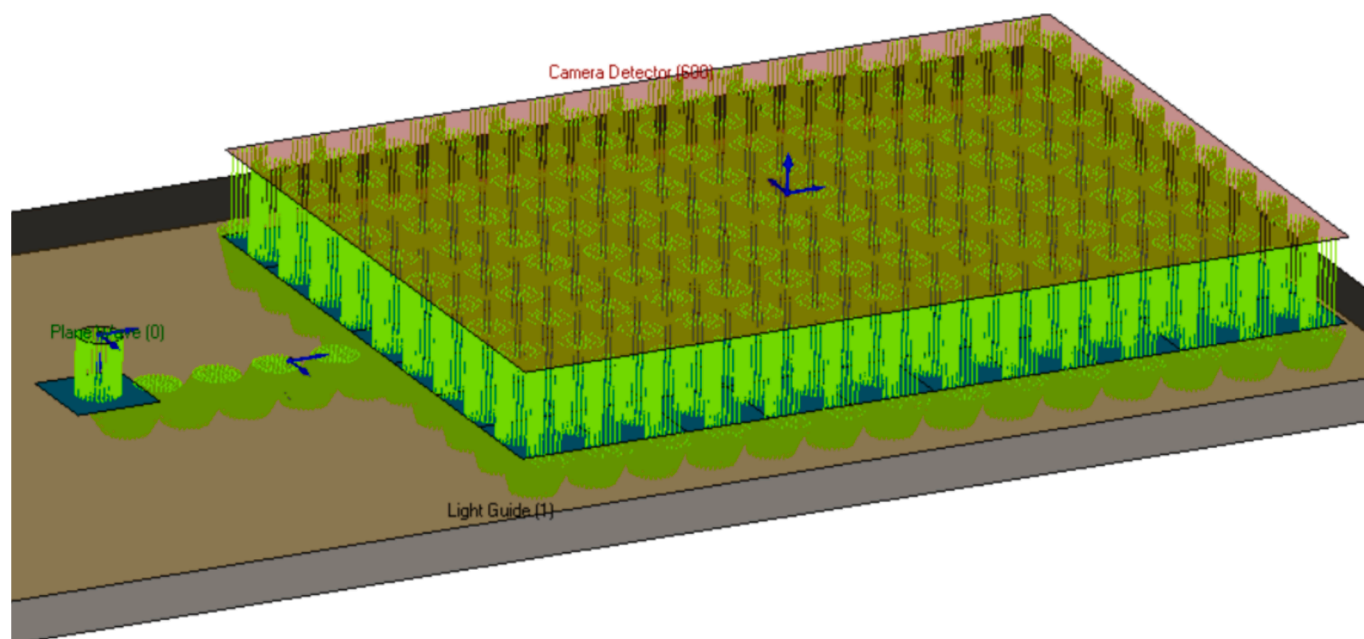


Fig. 14. Ray tracing diagram of channel 3. The wavelength is 546 nm. The incident angle is 0° . The waveguide thickness is 1.5 mm. The input pupil is a circle with a diameter of 3 mm. The size of ICG is $3 \times 3 \text{ mm}^2$. The size of OCG is $30 \times 21 \text{ mm}^2$. The distance between ICG and OCG is 9 mm.

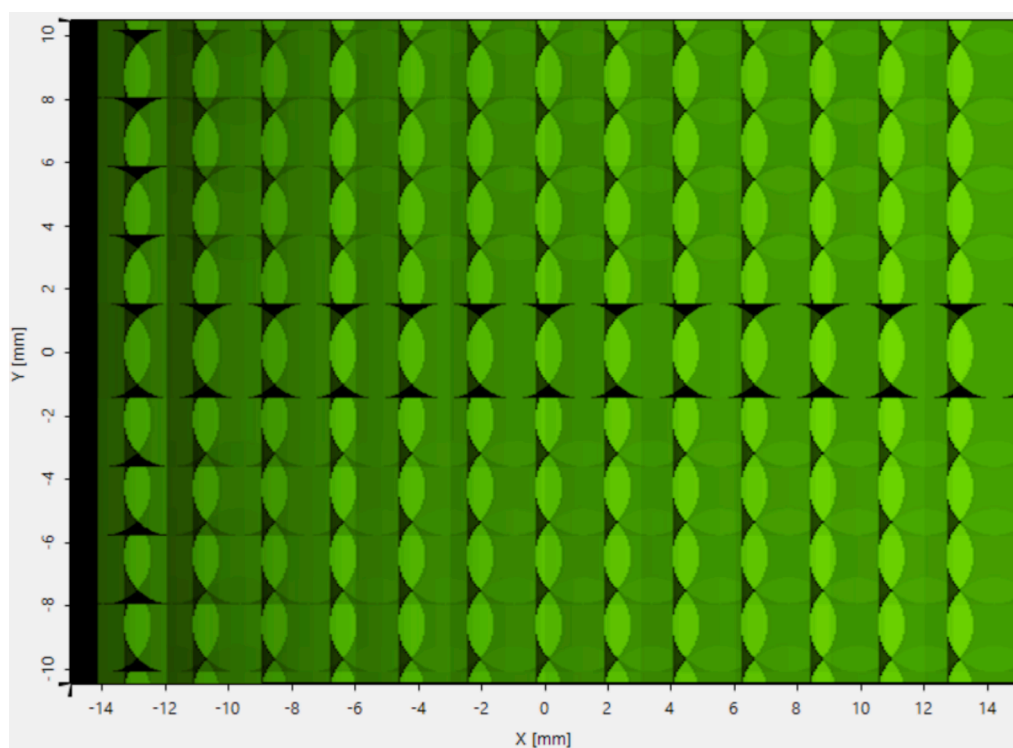


Fig. 15. Intensity map of duplicated pupils of channel 3. As the minimal and maximal intensities are 0.00026 and $0.00071 \text{ V}^2/\text{m}^2$, respectively, the pupil uniformity is 54 %.

CRediT authorship contribution statement

Chao Ping Chen: Conceptualization, Formal analysis, Investigation, Writing – original draft, Writing – review & editing, Supervision. **XiaoJun Wu:** Formal analysis, Software, Data curation. **Jinfeng Wang:** Investigation, Software. **Baoen Han:** Validation. **Yunfan Yang:** Validation. **Shuxin Liu:** Resources, Project administration, Funding acquisition.

Funding

This work is supported by Ministry of Industry and Information Technology of China (GO0300164/001), National Natural Science Foundation of China (62105203), and Natural Science Foundation of Chongqing Municipality (cstb2023nscq-msx0465).

Declaration of competing interest

The authors declare that they have no known competing financial interests or personal relationships that could have appeared to influence the work reported in this paper.

Acknowledgments

Special thanks to Yuepeng Cui (Shanghai InfoTek Science & Technology) for his technical support amid the waveguide simulation.

Data availability

Data will be made available on request.

References

- [1] R. Kuttappan, The rise and fall of the metaverse: a postmortem, <https://www.linkedin.com/pulse/rise-fall-metaverse-postmortem-rohit-kuttappan> (accessed 20 January 2025).
- [2] J. Glasner, Startup investors have fled the metaverse, <https://news.crunchbase.com/venture/startup-investors-metaverse-funding-falls-aapl> (accessed 20 January 2025).
- [3] L. Zhou, C.P. Chen, Y. Wu, Z. Zhang, K. Wang, B. Yu, Y. Li, See-through near-eye displays enabling vision correction, *Opt. Express* 25 (3) (2017) 2130–2142.
- [4] W. Zhang, C.P. Chen, H. Ding, L. Mi, J. Chen, Y. Liu, C. Zhu, See-through near-eye display with built-in prescription and two-dimensional exit pupil expansion, *Appl. Sci.* 10 (11) (2020) 3901.
- [5] H. Sun, *Lens Design: A Practical Guide*, CRC Press, Boca Raton, 2016.
- [6] B.C. Kress, *Optical Architectures for Augmented-, Virtual-, and Mixed-Reality Headsets*, SPIE, Bellingham, 2020.
- [7] Q. Hou, D. Cheng, Y. Li, T. Zhang, D. Li, Y. Huang, H. Chen, Q. Wang, W. Hou, T. Yang, Y. Wang, Stray light analysis and suppression method of a pancake virtual reality head-mounted display, *Opt. Express* 30 (25) (2022) 44918–44932.
- [8] Y. Ding, Z. Luo, G. Borjigin, S.-T. Wu, High-efficiency and ultracompact pancake optics for virtual reality, *J. Soc. Inf. Disp.* 32 (5) (2024) 341–349.
- [9] Y. Jeong, M. Choi, J. Choi, K. Kwak, Foveated pancake lens design for improved optical performance and eye rotation support, *Opt. Lett.* 49 (10) (2024) 2593–2596.
- [10] Y. Amitai, Extremely compact high-performance HMDs based on substrate-guided optical element, in: *SID Symposium Digest of Technical Papers*, Boston, 2004, pp. 310–313.
- [11] T. Levola, Diffractive optics for virtual reality displays, *J. Soc. Inf. Disp.* 14 (5) (2006) 467–475.
- [12] H. Mukawa, K. Akutsu, I. Matsumura, S. Nakano, T. Yoshida, M. Kuwahara, K. Aiki, A full-color eyewear display using planar waveguides with reflection volume holograms, *J. Soc. Inf. Disp.* 17 (3) (2009) 185–193.
- [13] Y. Wu, C.P. Chen, L. Zhou, Y. Li, B. Yu, H. Jin, Design of see-through near-eye display for presbyopia, *Opt. Express* 25 (8) (2017) 8937–8949.
- [14] B.T. Schowengerdt, D. Lin, P. St. Hilaire, Multi-layer diffractive eyepiece, US Patent Application 2018/0052277 A1, 2017.
- [15] J. Ha, J. Kim, Augmented reality optics system with pinpoint mirror, US Patent Application 2019/0204600 A1, 2017.
- [16] D. Grey, S. Talukdar, Exit pupil expanding diffractive optical waveguiding device, US Patent 10,359,635 B2, 2018.
- [17] Y. Weng, Y. Zhang, W. Wang, Y. Gu, C. Wang, R. Wei, L. Zhang, B. Wang, High-efficiency and compact two-dimensional exit pupil expansion design for diffractive waveguide based on polarization volume grating, *Opt. Express* 31 (4) (2023) 6601–6614.
- [18] M. Broadway, What is the Apple Vision Pro FOV? Here's what we know, <https://www.pcguides.com/vr/apple-vision-pro-fov/> (accessed 20 January 2025).
- [19] T. Vallius, J. Tervo, Waveguides with extended field of view, US Patent 9,791,703 B1, 2016.
- [20] Z. Shi, W.T. Chen, F. Capasso, Wide field-of-view waveguide displays enabled by polarization-dependent metagratings, *Proc. SPIE* 10676 (2018) 1067615.
- [21] C. Yoo, K. Bang, M. Chae, B. Lee, Extended-viewing-angle waveguide near-eye display with a polarization-dependent steering combiner, *Opt. Lett.* 45 (10) (2020) 2870–2873.
- [22] C.P. Chen, L. Mi, W. Zhang, J. Ye, G. Li, Waveguide-based near-eye display with dual-channel exit pupil expander, *Displays* 67 (2021) 101998.
- [23] C.P. Chen, L. Mi, W. Zhang, J. Ye, G. Li, Wide-field-of-view near-eye display with dual-channel waveguide, *Photonics* 8 (12) (2021) 557.
- [24] C.P. Chen, Y. Cui, Y. Chen, S. Meng, Y. Sun, C. Mao, Q. Chu, Near-eye display with a triple-channel waveguide for metaverse, *Opt. Express* 30 (17) (2022) 31256–31266.
- [25] C.P. Chen, X. Ma, S.P. Zou, T. Liu, Q. Chu, H. Hu, Y. Cui, Quad-channel waveguide-based near-eye display for metaverse, *Displays* 81 (2023) 102582.
- [26] Sony Semiconductor Solutions Group, OLED Microdisplay, <https://www.sony-semicon.com/en/products/microdisplay/oled.html> (accessed 20 January 2025).
- [27] E. Chen, Z. Yao, Z. Fan, W. Lai, T. Liang, Q. Yan, T. Guo, C.P. Chen, Collimated LED array with mushroom-cap encapsulation for near-eye display projection engine, *IEEE J. Sel. Top. Quantum Electron.* 30 (2) (2024) 2000410.
- [28] J. Gao, P. Chen, L. Wu, B. Yu, L. Qian, A review on fabrication of blazed gratings, *J. Phys. d: Appl. Phys.* 54 (31) (2021) 313001.
- [29] M. Oliva, T. Harzendorf, D. Michaelis, U.D. Zeitner, A. Tunnermann, Multilevel blazed gratings in resonance domain: an alternative to the classical fabrication approach, *Opt. Express* 19 (15) (2011) 14735–14745.
- [30] M.G. Moharam, T.K. Gaylord, Rigorous coupled-wave analysis of planar-grating diffraction, *J. Opt. Soc. Am.* 71 (7) (1981) 811–818.
- [31] Wikipedia, Circle packing, https://en.wikipedia.org/wiki/Circle_packing (accessed 20 January 2025).
- [32] C.P. Chen, Y. Su, C.G. Jhun, Recent advances in holographic recording media for dynamic holographic display, *J. Opt. Photonics* 1 (2014) 1–8.
- [33] Q. Ji, H. Deng, H. Zhang, W. Jiang, F. Zhong, F. Rao, Optical see-through 2D/3D compatible display using variable-focus lens and multiplexed holographic optical elements, *Photonics* 8 (8) (2021) 297.
- [34] Z.-H. He, C.-P. Chen, J.-L. Zhu, Y.-C. Yuan, Y. Li, W. Hu, X. Li, H.-J. Li, J.-G. Lu, Y.-K. Su, Electrically tunable holographic polymer templated blue phase liquid crystal grating, *Chin. Phys. B* 24 (6) (2015) 064203.
- [35] Z. Zhang, C.P. Chen, Y. Li, B. Yu, L. Zhou, Y. Wu, Angular multiplexing of holographic display using tunable multi-stage gratings, *Mol. Cryst. Liq. Cryst.* 657 (1) (2018) 102–106.
- [36] J.E. Melzer, K. Moffitt, *Head-Mounted Displays: Designing for the User*, McGraw-Hill, New York, 1997.
- [37] Q. Li, W. He, H. Deng, F.-Y. Zhong, Y. Chen, High-performance reflection-type augmented reality 3D display using a reflective polarizer, *Opt. Express* 29 (6) (2021) 9446–9453.
- [38] C.-C. Wu, K.-T. Shih, J.-W. Huang, H.H. Chen, A novel birdbath eyepiece for light field AR glasses, *Proc. SPIE* 12449 (2023) 124490N.
- [39] L. Jiang, J. Lin, F. Rao, Q. Li, Y. Fu, H. Deng, Dual-mode optical see-through integral imaging 3D display with large depth of field, *Opt. Lasers Eng.* 175 (2024) 107986.
- [40] R. Sprague, A. Zhang, L. Hendricks, T. O'Brien, R. Collins, J. Ford, E. Tremblay, T. Rutherford, Novel HMD concepts from the DARPA SCENICC program, *Proc. SPIE* 8383 (2012) 838302.
- [41] Y. Wu, C.P. Chen, L. Mi, W. Zhang, J. Zhao, Y. Lu, W. Guo, B. Yu, Y. Li, N. Maitlo, Design of retinal-projection-based near-eye display with contact lens, *Opt. Express* 26 (9) (2018) 11553–11567.
- [42] J. Chen, L. Mi, C.P. Chen, H. Liu, J. Jiang, W. Zhang, Design of foveated contact lens display for augmented reality, *Opt. Express* 27 (26) (2019) 38204–38219.